Journal of Materials Chemistry C

Accepted Manuscript

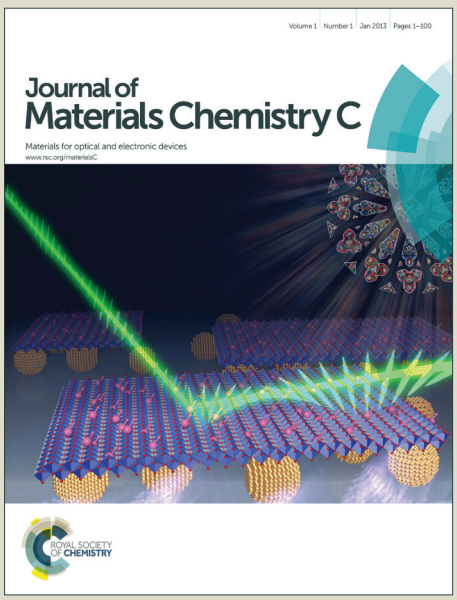

ROYAL SOCIETY OF CHEMISTRY

www.rsc.org/materialsC

Journal of Materials Chemistry C

PAPER

The Effect of Light Rare Earth Elements Substitution in $Yb_{14}MnSb_{11}$ on Thermoelectric Properties

Yufei Hu,[a] Sabah K. Bux,[b] Jason H. Grebenkemper,[a] and Susan M. Kauzlarich*[a]

Received 00th January 20xx,
Accepted 00th January 20xx

DOI: 10.1039/x0xx00000x

www.rsc.org/

After the discovery of $Yb_{14}MnSb_{11}$ as an outstanding *p*-type thermoelectric material for high temperatures (≥ 900 K), site substitution of other elements has been proven to be an effective method to further optimize the thermoelectric properties. $Yb_{14-x}RE_xMnSb_{11}$ (*RE* = Pr and Sm, $0 < x < 0.55$) were prepared by powder metallurgy to study their thermoelectric properties. According to powder X-ray diffraction, these samples are iso-structural with $Yb_{14}MnSb_{11}$ and when more than 5 % *RE* is used in the synthesis the presence of $(Yb,RE)_4Sb_3$ is apparent after synthesis. After consolidation and measurement, (Yb,*RE*)Sb and $(Yb,RE)_{11}Sb_{10}$ appear in the powder X-ray diffraction patterns. Electron microprobe results show that consolidated pellets have small (Yb,*RE*)Sb domains and that the maximum amount of *RE* in $Yb_{14-x}RE_xMnSb_{11}$ is $x = 0.55$, however, $(Yb,RE)_{11}Sb_{10}$ can not distinguished by electron microprobe. By replacing Yb^{2+} with RE^{3+}, one extra electron is introduced into $Yb_{14}MnSb_{11}$ and carrier concentration adjusted. Thermoelectric performance from room temperature to 1275 K was evaluated through transport and thermal conductivity measurements. The measurement shows that Seebeck coefficients initially increase and then remain stable and that electrical resistivity increases with substitutions. Thermal conductivity is slightly reduced. Substitutions of Pr and Sm lead to enhanced *zT*. $Yb_{13.82}Pr_{0.18}Mn_{1.01}Sb_{10.99}$ has the best maximum *zT* value of ~1.2 at 1275 K, while $Yb_{13.80}Sm_{0.19}Mn_{1.00}Sb_{11.02}$ has its maximum *zT* of ~1.0 at 1275 K, respectively ~45% and ~30% higher than $Yb_{14}MnSb_{11}$ prepared in the same manner.

1. Introduction

The great demand for energy and consumption of fossil fuels have propelled research on energy conversion materials, since combustion of fossil fuels provides wasted heat that could be converted into useful energy.[1] Therefore, thermoelectric materials, which can directly convert heat into electricity, have been undergoing a renewed prosperity. As sustainable, reliable and flexible energy sources, thermoelectric materials have successfully been applied to Radioisotope Thermoelectric Generators (RTGs) for space explorations and to remote power such as oil pipelines and deep sea detection.[2,3] The efficiency of a thermoelectric material can be evaluated by the dimensionless figure of merit (*zT*) using Equation (1):

$$zT = \alpha^2\sigma T / \kappa \quad (1)$$

where α represents Seebeck coefficient ($\Delta V/\Delta T$), σ represents electrical conductivity, *T* represents the average temperature and κ represents thermal conductivity.[4] According to the equation, a high efficiency thermoelectric material should have three characteristics: a high Seebeck coefficient, high electrical conductivity and low thermal conductivity.

The highest peak *zT* value reported to date is 2.6 at 923 K discovered in the study of SnSe crystals, while several other systems were reported to possess peak *zT* values larger than 2 in bulk phases.[5-8] In general, materials that are considered to be superior for thermoelectric applications have maximum *zT* values around 1 to 1.5, although great efforts have been made to optimize existing thermoelectric materials, discover new ones and improve average *zT*. The difficulty of improving *zT* values in thermoelectric materials lies in the fact that the three variables (Seebeck coefficient, electrical resistivity and thermal conductivity) are related to each other and more or less dependent on carrier concentration. Electrical resistivity and Seebeck coefficient (assuming a single parabolic model) can be presented by Equation (2) and (3):

$$\sigma = ne\mu \quad (2)$$

$$\alpha = 8\pi^2 k_B^2 m^* T \times (\pi/3n)^{2/3} / 3eh^2 \quad (3)$$

where *n* represents carrier concentration, μ represents mobility, m^* is the effective mass of carriers, k_B is the Boltzman constant and *h* is the Planck's constant.[9] Thus, a high electrical conductivity relies on a large carrier concentration and a high carrier mobility. Meanwhile, a high Seebeck coefficient relies on a large effective mass of carriers and a small carrier concentration. The reverse effect of carrier concentrations on electrical resistivity and Seebeck coefficient requires a careful control of carrier concentrations to optimize thermoelectric materials and achieve high *zT* values. Generally speaking, semiconductors can meet aforementioned requirements due to

[a] Department of Chemistry, University of California, One Shields Avenue, Davis, California 95616, United States.
[b] Jet Propulsion Laboratory, California Institute of Technology, 4800 Oak Grove Drive, Pasadena, California 91109-8099, United States.

† Electronic Supplementary Information (ESI) available: [PXRD patterns of $Yb_{14-p}RE_pMnSb_{11}$ (RE = Pr and Sm, p = 0.2, 0.4, 0.6, 0.7, 0.8, 0.9, 1.0), element maps, refined PXRD patterns of $Yb_{13.82}Pr_{0.18}Mn_{1.01}Sb_{10.99}$, $Yb_{13.59}Pr_{0.34}Mn_{1.00}Sb_{11.08}$, $Yb_{13.53}Pr_{0.45}Mn_{1.02}Sb_{10.99}$, $Yb_{13.45}Pr_{0.55}Mn_{1.03}Sb_{10.97}$, $Yb_{13.80}Sm_{0.19}Mn_{1.00}Sb_{11.02}$ and $Yb_{13.50}Sm_{0.53}Mn_{1.06}Sb_{10.89}$ before SPS and after measurement, and specific heat capacity of samples (PDF)]. See DOI: 10.1039/x0xx00000x

its medium carrier concentration and the balance between Seebeck coefficient and electrical resistivity. Considering thermal conductivity, the effect of carrier concentration is more complex. Thermal conductivity is a sum of electronic κ_e, lattice κ_l and bipolar κ_b terms. Among the three terms, electronic term is related to electrical conductivity:

$$\kappa = \kappa_e + \kappa_l + \kappa_b \quad (4)$$

$$\kappa_e = L\sigma T \quad (5)$$

where L is Lorenz number.[9] Therefore, a large carrier concentration will also increase thermal conductivity and the other two terms of thermal conductivity make it difficult to improve zT through tuning carrier concentration. A simulation of Bi_2Te_3 shows that an optimum zT value is achieved when carrier concentration is appropriately adjusted.[9,10]

Another way to improve thermoelectric materials is to decrease lattice thermal conductivity. Slack proposed a corresponding concept "Phonon Glass Electron Crystal" (PGEC), which specifies that a good thermoelectric material should behave like glass to scatter phonons without significant disruption of electrons transportation.[4] Intrinsic low lattice thermal conductivity can be found in compounds owning heavy elements and complex unit cells, such as clathrates, skutterudites and Zintl phases.[11-13] Site disorders and substitutions can decrease lattice thermal conductivity further.

As a Zintl phase compound, $Yb_{14}MnSb_{11}$ (Fig. 1) well illustrates the PGEC concept.[14-16] This compound crystalizes in the space group of $I4_1/acd$ and one unit cell contains eight formula units. Each formula unit contains fourteen Yb^{2+} cations, one $[MnSb_4]^{9-}$ tetrahedron, one linear Sb_3^{7-} anion and four isolated Sb^{3-} anions. The Mn in $[MnSb_4]^{9-}$ tetrahedron was found to be divalent and thus an electron hole is present, making $Yb_{14}MnSb_{11}$ a p-type thermoelectric material.[17] Calculations on the band structures of its iso-structural analogs also support this interpretation.[18,19] $Yb_{14}MnSb_{11}$ is the best p-type thermoelectric material in the high temperature region so far and has a zT value of ~1 at 1200K owing to its low thermal conductivity(less than 1 W/ (m•K)) as well as its reasonable Seebeck coefficient and resistivity. Its potential applications for RTGs have been studied.[2,20,21]

To optimize the thermoelectric properties of $Yb_{14}MnSb_{11}$, studies have been carried out by employing solid solutions of various substituents.[22-30] Seebeck coefficient and electrical conductivity may be tuned due to the change of carrier concentration. Lattice thermal conductivity will also decrease because of the introduction of different atoms.[4] Substitutions on the Sb site have limited choices and Ge and Te only substitute a trace amount of Sb into the structure.[22,23] Mn can form solid solution with Zn and Al, while on the Yb site, La, Tm and Lu are found to form limited solid solutions (less than 5%) and Ca forms a full solid solution.[24-30] The effects of these four elements on thermoelectric properties are different. When trivalent La and Tm substitutes Yb, one more electron is donated to the structure to decrease the carrier (holes) concentration, leading to a higher Seebeck coefficient, a higher electrical resistivity and a lower thermal conductivity.[27,28] Ca has similar effects since Ca is more electropositive than Yb and can transfer electrons more completely to the structure, although both Yb and Ca are divalent. The Lu substitution of La, Tm and Ca can also decrease lattice thermal conductivity due to the addition of different atoms. However, Lu substitution has a reverse effect and the reason is unclear.[29]

Despite the aforementioned research, many possible substituents remain unstudied. As in the case of skutterudites where different rare earth elements lead to distinct properties, other rare earth elements substitution for Yb may also provide variable results.[31-34] In order to explore more possibilities to optimize $Yb_{14}MnSb_{11}$ and systematically study the effect of substituting Yb with rare earth elements on thermoelectric properties, the solid solutions $Yb_{14-x}RE_xMnSb_{11}$ (RE = Pr and Sm, $0 < x < 0.55$) were synthesized and their thermoelectric properties were measured. Thermoelectric properties of Pr substituted samples will be presented and discussed and then compared with Sm substituted samples.

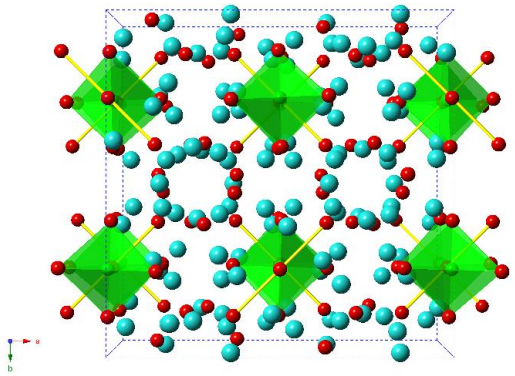

Figure 1. Unit cell of $Yb_{14}MnSb_{11}$ projected along c direction. Blue spheres represent Yb atoms, green tetrahedra represent $[MnSb_4]^{9-}$, red spheres represent Sb atoms and Sb_3^{7-} is shown with yellow bonds.

2. Experimental Details

2.1 Synthesis

Elemental Yb pieces (Metall Rare Earth Limited, 99.99%), Pr pieces (Ames Lab, 99.99%), Sm pieces (Ames Lab, 99.99%), Mn pieces (Alfa Aesar, 99.95%) and Sb shots (Alfa Aesar, 99.999%) were used for synthesis. Yb, Pr, Sm and Mn were cut into small pieces (~1 mm^3) and Sb was used as received. All elements were handled in an argon filled drybox with water levels < 0.5 ppm. Powder samples were synthesized through a powder metallurgy method using a melt of "Mn+11Sb" as precursor. The elements were loaded at the ratio of Yb: RE: Mn: Sb = 14-p: p: 1: 11 (p = 0.2, 0.4, 0.6, 0.7, 0.8, 0.9, 1. p is the preparative amount of rare earth elements used in the synthesis. It is different from the experimentally determined amount in the product, represented by x). Mn and Sb were loaded into a 50 cm^3 WC ball mill container with one large WC ball (diameter = 11 mm) and two small balls (diameter = 8 mm) and ball milled on a SPEX 8000 M mixer/mill for 15 minutes. The mixture was then transferred into a BN crucible and sealed in a fused silica tube under vacuum. The silica tube was annealed at 1025 K for 3 days. The melted chunk was then ball milled for 15 minutes into fine powder, mixed with Yb and Pr or Sm, and ball milled again for 3 hours with 15 minutes on-and-off mode. Afterwards,

5 grams powder was transferred into a ~7 cm long niobium tube (inner diameter = 7 mm), where one end had been clamped and sealed in an arc welder under argon. Then the other end of the niobium tube was also clamped and sealed in the arc welder. Afterwards, the tube was sealed in a fused silica jacket under ¼ atmosphere pressure and annealed under 1375 K for 7 days. The reactions were opened in a glovebox and dark grey powder was harvested.

2.2 Powder X-ray Diffraction

Powder X-ray diffraction (PXRD) data were collected on each sample using a Bruker zero background holder on a Bruker D8 Advance Diffractometer operated at 40 kV and 40 mA utilizing Cu *Kα* radiation. *Kβ* radiation is cut off by a Ni filter. WinPLOTR (version Jan 2012) software was used for background subtraction and pattern analysis and EDPCR 2.00 software was used to perform fitting.[35,36]

2.3 Consolidation of Powder

Bulk powder samples were consolidated into dense pellets via a Dr. Sinter SPS-2050 spark plasma sintering (SPS) system (Sumitomo, Tokyo, Japan) in a 12.7 mm high-density graphite dies (POCO) under vacuum (<10 Pa). The temperature was increased from room temperature to 1000 K in 5 minutes, and remained stable for 10 minutes. When the temperature reached the maximum, the force increased from 3 kN to 6-7 kN. Afterwards samples were cooled to room temperature with pressure released. Sample densities were larger than 97% of the theoretical density.

2.4 Electron Microprobe Analysis

Small pieces of consolidated pellets were analyzed using a Cameca SX-100 Electron Probe Microanalyzer equipped with a wavelength-dispersive spectrometer with 20 keV accelerating potential and 20 nA beam current. The samples were mounted in epoxy and polished to a smooth surface. The epoxy and sample were coated by carbon for better conduction. X-ray elemental maps were taken at a representative area for each sample. Net elemental intensities for Yb, Mn, and Sb were determined with respect to crystals of $Yb_{14}MnSb_{11}$, and $PrPO_4$ and $SmPO_4$ was respectively used as standards for net elemental intensities of Pr and Sm. The composition of each sample was determined by calculating averages and standard deviations from at least 10 randomly selected data points of the main phase. The amounts of Pr and Sm determined by electron microprobe are different from the amounts used in synthesis.

2.5 Electrical Resistivity, Hall Effect and Seebeck Coefficient

The van der Pauw technique was used to measure the electrical resistivity (ρ) with a current of 100 mA in a special high-temperature apparatus.[37] The Hall coefficient was measured simultaneously on the same instrument utilizing a forward and reverse magnetic field value of about 7480 G. The charge carrier density (n) was calculated from the Hall coefficient (R_H) assuming a scattering factor of 1.0 in a single-carrier scheme, with $n = 1/R_H e$, where e is the charge of the electron. The uncertainty of resistivity is ± 5 %.[5,38,39] The Seebeck coefficient (α) was measured in a graphite heater using W/Nb thermocouples with light pulses to create a temperature difference.[40] The uncertainty of Seebeck coefficient is ± 5 %.[5,38,39] All data were collected to 1275 K, and fit into six order polynomial functions for *zT* calculations.

2.6 Thermal Conductivity

Thermal diffusivity (D) from 300 K to 1275 K was measured on the pellets obtained from SPS in a Netzsch LFA-457 unit.[41] The pellet surfaces were well polished and coated with graphite. The measurement was conducted under high vacuum. Thermal conductivity was calculated using the equation $\kappa = D \times d \times C_p$, where d is the density and Cp is the heat capacity at constant pressure. Room-temperature density was measured with geometric method and high-temperature density was derived using thermal expansion data from a previous paper on $Yb_{14}MnSb_{11}$.[42] The C_p was also estimated from a previous paper.[25] The uncertainty of thermal conductivity is ± 5 % and the total uncertainty of zT is ± 10 %.[5,38]

3. Results and Discussion

3.1 PXRD Patterns after Synthesis

Samples of $Yb_{14-p}RE_pMnSb_{11}$ (*RE* = Pr and Sm, p = 0.2, 0.4, 0.6, 0.7, 0.8, 1.0) where p is the preparative amount, were synthesized by ball milling the elements and annealing at 1375 K for 7 days. For samples with *RE* = Pr and $p \geq 0.7$, an impurity phase $(Yb,Pr)_4Sb_3$ could be identified in the PXRD patterns (Supporting Information). For the samples with $p < 0.7$, unit cell parameters increase with increasing Pr amount based on refinement (Table 1.). Although Pr^{3+} (0.99 Å) is smaller than Yb^{2+} (1.02 Å), the increase of unit cell parameters may be attributed to the change of bond angles and bond lengths in $[MnSb_4]^{9-}$ caused by substitution.[18,43,44] For the samples with $(Yb,Pr)_4Sb_3$, the secondary phase was considered in the refinement. Unit cell parameters remained approximately the same after reaching the maximum at p = 0.7. Meanwhile, the peak intensity of $(Yb,Pr)_4Sb_3$ increased when p is larger than 0.7. Therefore, the substitution of Pr enlarges the unit cell, and a secondary phase $(Yb,Pr)_4Sb_3$ forms when the synthetic amount of Pr exceeds 0.7.[44] Attempts were made to remove the secondary phase $(Yb,Pr)_4Sb_3$ by annealing for longer time at high temperature. However, the attempts failed presumably because Yb_4Sb_3 is the

Table 1. Unit cell parameters of $Yb_{14-p}RE_pMnSb_{11}$ (*RE* = Pr and Sm, p = 0.2, 0.4, 0.6, 0.7, 0.8, 0.9, 1)

p	a (Å)	c (Å)	c/a	V (Å^3)
		$Yb_{14-p}Pr_pMnSb_{11}$		
0	16.6106(1)	21.9962(2)	1.3243	6069.0(1)
0.2	16.6220(1)	22.0017(2)	1.3236	6078.6(1)
0.4	16.6323(1)	22.0223(2)	1.3241	6092.1(1)
0.6	16.6471(1)	22.0383(2)	1.3238	6107.4(1)
0.7	16.6519(1)	22.0439(2)	1.3238	6112.5(1)
0.8	16.6471(1)	22.0398(2)	1.3240	6107.8(1)
1	16.6509(1)	22.0371(2)	1.3235	6109.8(1)
		$Yb_{14-p}Sm_pMnSb_{11}$		
0.2	16.6213(1)	22.0159(2)	1.3246	6082.3(1)
0.4	16.6249(1)	22.0272(2)	1.3250	6088.0(1)
0.6	16.6336(1)	22.0411(2)	1.3251	6098.3(1)
0.8	16.6375(1)	22.0511(2)	1.3254	6103.9(1)
0.9	16.6413(1)	22.0539(2)	1.3253	6107.4(1)
1	16.6397(1)	22.0606(2)	1.3258	6108.1(1)

most stable binary compound between ytterbium and antimony stable up to 1900 K.[45] For $Yb_{14-p}Sm_pMnSb_{11}$ (p = 0.2, 0.4, 0.6, 0.7, 0.8, 0.9, 1.0), a similar trend was observed. When p exceeds 0.9, impurity phases appears and unit cell parameters reach their maximum. When the same amount of Yb was substituted, the Pr containing sample has a larger unit cell volume than the Sm phase, since Pr^{3+} has a larger size than Sm^{3+}. Samples with $p \leq 0.8$ were consolidated by SPS for transport and thermal conductivity measurements.

3.2 Electron Microprobe and PXRD Patterns after Measurement

Dense pellets ($p \leq 0.8$) were examined by electron microprobe analysis and elemental mapping images (Supporting Information) showed inhomogeneous distributions, most clearly seen in the *RE* elemental maps. The experimental compositions of these pellets were calculated from WDS data points measured on homogeneous matrix and listed in Table 2. The measured Pr amounts in the matrix, x, are smaller than the amount used in the synthesis, p. When p = 0.6, the experimental amount reaches the maximum of x = 0.55 and when p = 0.8, the measured amount drops to x = 0.45. Pr and Sb rich regions increase with increasing Pr amount and correspondingly, Yb relative compositions are low in these regions. This phase is determined to be (Yb,Pr)Sb and leads to lower values of x for $Yb_{14-x}RE_xMnSb_{11}$ than the preparative amount, p. Since the microprobe was performed after transport and thermal conductivity measurements, this impurity must form either during consolidation or measurement. Some Yb rich regions are also observed and by comparing with other elements, these regions should be Yb_2O_3. Only two Sm substituted samples (p = 0.2 and 0.8) were examined and they show the same tendency, i.e. the experimental value, x, is lower than the preparative amount, p, and impurities can be discerned in the elemental mapping images and in the PXRD. In the discussion of resistivity, Seebeck coefficient, thermal conducitivity and zT, experimental compositions, x values, will be used.

After transport measurements, pellets were ground into powder and tested by PXRD (Supporting Information). Peaks of (Yb,*RE*)Sb and $(Yb,RE)_{11}Sb_{10}$ were observed.[46,47] It is difficult to identify $(Yb,RE)_{11}Sb_{10}$ from PXRD as its peaks overlap with $Yb_{14}MnSb_{11}$ but the refinement improved with the inclusion of $Yb_{11}Sb_{10}$ as a component. $(Yb,RE)_{11}Sb_{10}$ is not apparent by electron microprobe, presumably because it does not provide sufficient contrast to $Yb_{14}MnSb_{11}$ and is present in small amounts. The thermoelectric properties of $(Yb,RE)_{11}Sb_{10}$ and YbSb have been studied.[18,48,49] These two compounds have small Seebeck coefficients and low resistivity. These small domains should have little effect on the Seebeck coefficient and resistivity of $Yb_{14}MnSb_{11}$, however, these impurities will add more grain boundaries in the pellets which will increase resistivity and therefore decrease thermal conductivity. The formation of these impurities may also cause the bend-over of resistivity in the highest temperature region (vide infra).[50]

3.3 Electrical resistivity

Figure 2 shows electrical resistivity of $Yb_{14-x}Pr_xMnSb_{11}$ (x = 0.18, 0.34, 0.45, 0.55). The resistivity increases from 2 mΩ•cm at room temperature to 6-7.5 mΩ•cm at 1275 K. All samples possess linearly increasing resistivity in the low temperature region, indicating heavily doped semiconducting properties of these samples. Around 1100 K, the resistivity increases more slowly with temperature attributed to both a bipolar effect caused by excitation of carriers at high temperatures and the presence or formation of the impurities. The resistivity goes up with x values except for x = 0.45 (p = 0.8), which has the most impurities with (Yb,*RE*)Sb, $(Yb,RE)_{11}Sb_{10}$ and $(Yb,RE)_4Sb_3$. In general, more Pr substitution amount leads to higher resistivity because Pr^{3+} can donate one more electron than Yb^{2+} and the electron fills the hole to decrease carrier concentration. However, the x = 0.45 sample has the highest resistivity because the increased amount of impurities compared with x = 0.55 add more grain boundaries which scatter electrons and increase resistivity. Compared with other optimized $Yb_{14}MnSb_{11}$ systems, Pr substituted samples have smaller resistivity than La substituted $Yb_{14}MnSb_{11}$ but higher values than Ca substituted samples.[27,30]

Table 2. Carrier concentration of $Yb_{14-x}RE_xMnSb_{11}$ and amount of *RE* from calculation and measurement

p	Compositions from electron microprobe analysis	Measured Carrier concentration (10^{20}/cm^3)	Estimated carrier concentration (10^{20}/cm^3)
	$Yb_{14-x}Pr_xMnSb_{11}$		
0	--	10.1(1)	--
0.2	$Yb_{13.82(6)}Pr_{0.18(1)}Mn_{1.01(5)}Sb_{10.99(5)}$	6.3(1)	8.3
0.4	$Yb_{13.59(15)}Pr_{0.34(1)}Mn_{1.00(7)}Sb_{11.08(9)}$	5.7(1)	6.7
0.6	$Yb_{13.45(15)}Pr_{0.55(1)}Mn_{1.03(7)}Sb_{10.97(9)}$	5.2(1)	4.6
0.8	$Yb_{13.53(15)}Pr_{0.45(1)}Mn_{1.02(7)}Sb_{10.99(9)}$	5.3(1)	5.6
	$Yb_{14-x}Sm_xMnSb_{11}$		
0.2	$Yb_{13.80(5)}Sm_{0.19(1)}Mn_{1.00(1)}Sb_{11.02(7)}$	6.1(1)	8.2
0.8	$Yb_{13.50(7)}Sm_{0.53(1)}Mn_{1.06(2)}Sb_{10.89(9)}$	4.3(1)	4.8

The carrier concentrations of these samples fall into the range of 6.3~5.2 × 10^{20}/cm^3 (Table 2), matching with that of previous work.[27] A large drop in carrier concentration is observed between $Yb_{14}MnSb_{11}$ and $Yb_{13.82}Pr_{0.18}Mn_{1.01}Sb_{10.99}$. The amount x in formula unit is estimated to decrease the carrier concentration by x • (1 × 10^{21}/cm^3) (each Pr^{3+} contributes an additional electron compared with Yb^{2+}). Therefore, carrier concentrations can be calculated based on the compositions obtained by electron microprobe. For example, when x = 0.18, the carrier concentration is 10.1 – 0.18 • (1 × 10^{21}) = 8.3 ×

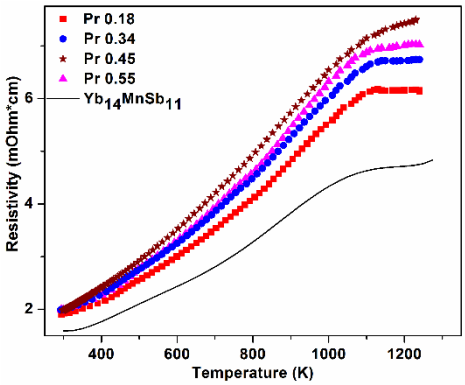

Figure 2. Electrical resistivity of $Yb_{14-x}Pr_xMnSb_{11}$ (x = 0.18, 0.34, 0.45, 0.55). The resistivity of $Yb_{14}MnSb_{11}$ synthesized by the same method is also shown in the plots.

10^{20}/cm^3. However, calculated carrier concentrations disagree with the results from experimental measurement for x = 0.18 and 0.34 and the carrier concentration is more reduced than can be accounted for by simply electron counting. This result suggests that the simple single parabolic band model is overly simplistic and that subtle changes in compositions, including the presence of the partially filled *4f*-orbitals of Pr may change the band structure at the top of valence band. This would account for the difference between calculated and experimental carrier concentration and the result is a larger reduction in the carrier concentrations at small x between substituted and pristine $Yb_{14}MnSb_{11}$. Considering $Yb_{14}Mn_{1-y}Al_ySb_{11}$ (y = 0.2, 0.4, 0.6, 0.8, 0.95, 1) compounds, in which a linear change of carrier concentrations is observed, substitutions on different sites will affect the band structure differently, leading to the observed changes in carrier concentrations and properties.[9,25] Another example of $Yb_{14}MnSb_{11-m}Te_m$ shows that a trace amount of Te on the Sb sites could increase the Seebeck coefficient and electrical resistivity dramatically.[23] Therefore, the effects of substitutions on the three sites (Yb, Mn and Sb) will indicate the sites' contributions to the band structure near the Fermi level. This can help understand the intrinsic electronic property of $Yb_{14}MnSb_{11}$ and provide guidance for further optimization of $Yb_{14}MnSb_{11}$ by multiple substitutions.

3.4 Seebeck coefficient

Figure 3a shows the measured curves of Seebeck coefficient of $Yb_{14-x}Pr_xMnSb_{11}$ (x = 0.18, 0.34, 0.45, 0.55). The differences are small and within the uncertainty. The Seebeck coefficient of all samples increase from ~40 μV/K at room temperature to 215~230 μV/K at high temperatures, close to that of $Yb_{13.6}La_{0.4}MnSb_{11}$ and higher than those of $Yb_{14-z}Ca_zMnSb_{11}$ (z = 1, 2, 4). Similar to electrical resistivity, the curves of Seebeck coefficient increase linearly in the low temperature region and reach maxima around 1100 K. The decline of Seebeck coefficient in the high temperature region is similar to that observed for resistivity and is attributed to both the bipolar effect and the presence or formation of the secondary phases. Pr substituted samples show much higher Seebeck coefficient than pristine $Yb_{14}MnSb_{11}$, which agrees with the lower carrier concentrations.

The effective band gap (E_g) of these samples (Fig 3b) can be estimated according to Equation (6):

$$E_g = 2 \times e \times \alpha_{max} \times T_{max} \quad (6)$$

where α_{max} is the peak Seebeck coefficient and T_{max} is the temperature at which the peak occurs.[51] The effective band gaps are close to reported values and are consistent with calculation results on iso-structural analogs.[18,19,26,52] Pr substituted samples have similar values while pristine $Yb_{14}MnSb_{11}$ has a smaller value. Considering the discussions on carrier concentration, this could also be attributed to possible change in band structure when Yb is substituted by Pr.

3.5 Thermal conductivity and *zT*

Thermal conductivities and *zT* values are presented in Figure 4.

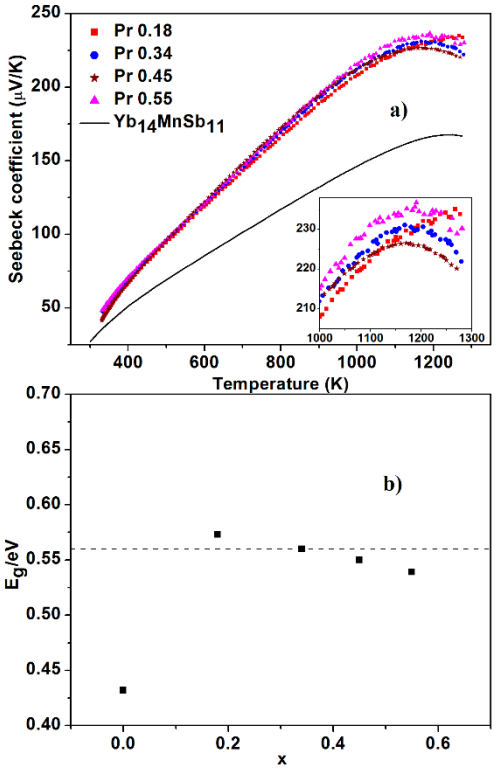

Figure 3. a) Seebeck coefficients and b) estimated band gaps of $Yb_{14-x}Pr_xMnSb_{11}$ (x = 0.18, 0.34, 0.45, 0.55). At the bottom right of a) is an enlarged plot for temperature between 1000 and 1250 K. Dashed lines are arbitrary lines for convenience. The values of $Yb_{14}MnSb_{11}$ synthesized by the same method are also shown in the plots.

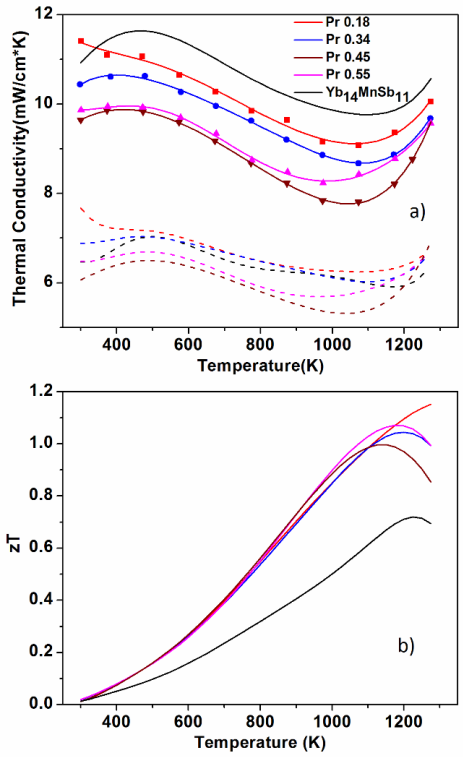

Figure 4. a) Total thermal conductivity and lattice thermal conductivity, and b) calculated zT values of $Yb_{14-x}Pr_xMnSb_{11}$ (x = 0.18, 0.34, 0.45, 0.55). Dots are measured values and solid curves are the polynomial fits. Dashed lines are the polynomial fits of the calculated lattice thermal conductivity. The values of $Yb_{14}MnSb_{11}$ synthesized by the same method are also shown in the plots.

These compounds have low and similar thermal conductivity that slightly decreases with Pr substitutions. The addition of lattice and bipolar thermal conductivities were calculated using Equation (4) and (5), and Lorenz numbers were calculated from measured Seebeck coefficient according to Equation (7) and Equation (8):

$$L = (k_B/e)^2 \times [3F_0(\eta)F_2(\eta)-4F_1(\eta)^2]/F_0(\eta)^2 \quad (7)$$

$$\alpha = (k_B/e) \times [2F_1(\eta)/F_0(\eta)-\eta] \quad (8)$$

Where η is the reduced Fermi level and $F_n(\eta)$ is the Fermi-Dirac integral.[53,54] The Lorenz number is calculated to be ~2.3 × 10^{-8} W • Ω/K^2 at room temperature, approaching the value for free electrons (2.44 × 10^{-8} W • Ω/K^2), while the values are ~1.6× 10^{-8} W • Ω/K^2 at high temperatures. The lattice and bipolar thermal conductivities are calculated to be within the rang of 6-8 mW/(cm • K) and the increase at high temperature is attributed to bipolar effect, consistent with the experimental Seebeck coefficients and electrical resistivity. The small substitution of Pr has little effect on lattice thermal conductivity while large substitution of Pr obviously lowers the lattice thermal conductivity, which agrees with the PGEC concept. The presence of impurities as the amount of Pr increases will also help decrease thermal conductivity. Compared with electronic thermal conductivity, lattice and bipolar thermal conductivity contributes more to total thermal conductivity. The drops in both electronic and lattice thermal conductivity contribute to the drop of total thermal conductivity. Generally speaking, thermal conductivity of these samples are within previously reported range since the intrinsic complex structure leads to low thermal conductivity which is difficult to dramatically decrease.

Among all the samples, $Yb_{13.82}Pr_{0.18}Mn_{1.01}Sb_{10.99}$ has the largest peak zT values of 1.2 at 1275 K. $Yb_{13.59}Pr_{0.34}Mn_{1.00}Sb_{11.08}$ and $Yb_{13.45}Pr_{0.55}Mn_{1.03}Sb_{10.97}$ have close zT values whose peaks are between 1.0-1.1 at 1200 K. $Yb_{13.53}Pr_{0.45}Mn_{1.02}Sb_{10.99}$ has the smallest zT values and the peak at 1100 K reaches 1.0. $Yb_{13.82}Pr_{0.18}Mn_{1.01}Sb_{10.99}$ has a higher maximum zT value than previously reported optimized $Yb_{14}MnSb_{11}$ systems using the same experimental heat capacity adjusted for composition (Supporting Information).[25,26] Considering the inhomogeneity of the pellets, even higher zT values may be possible if phase pure pellets can be prepared.

3.5 Comparison between Pr and Sm substitution

Figure 5 shows the thermoelectric properties of $Yb_{13.82}Pr_{0.18}Mn_{1.01}Sb_{10.99}$, $Yb_{13.45}Pr_{0.55}Mn_{1.03}Sb_{10.97}$, $Yb_{13.80}Sm_{0.19}Mn_{1.00}Sb_{11.02}$ and $Yb_{13.50}Sm_{0.53}Mn_{1.06}Sb_{10.89}$. The compositions were chosen in order to compare both low and high substitution level. $Yb_{13.80}Sm_{0.19}Mn_{1.00}Sb_{11.02}$ and $Yb_{13.82}Pr_{0.18}Mn_{1.01}Sb_{10.99}$ almost have the same resistivity while $Yb_{13.50}Sm_{0.53}Mn_{1.06}Sb_{10.89}$ has a larger resistivity than $Yb_{13.45}Pr_{0.55}Mn_{1.03}Sb_{10.97}$. Similar carrier concentrations for the same substitution amount confirmed the resistivity and the differences in the x ~ 0.5 resistivity may be attributed to differences in microstructure. Seebeck coefficients as well as effective band gaps display similar values and tendencies within the four compositions. Thermal conductivity of Sm substituted samples is lower than that of Pr substituted samples and the

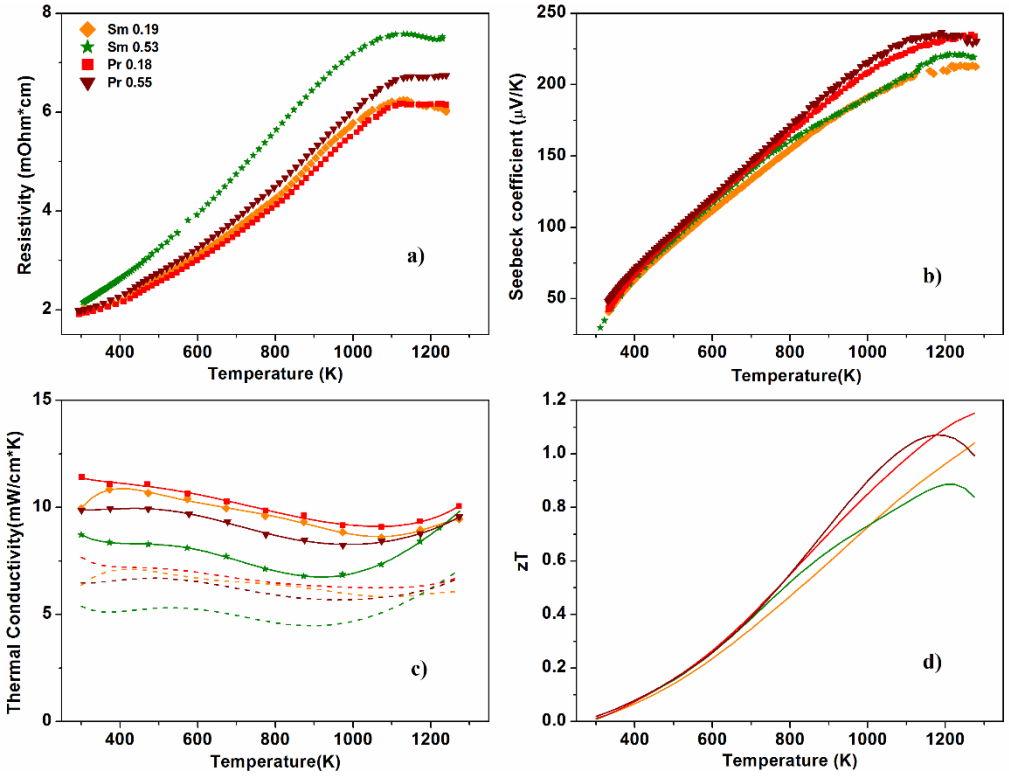

Figure 5. a) Electrical resistivity, b) Seebeck coefficient, c) total thermal conductivity and lattice thermal conductivity, d) calculated zT values of $Yb_{14-x}RE_xMnSb_{11}$ (RE = Pr and Sm). Dots are measured values and solid curves are the polynomial fits of measured dots. Dashed lines in c) are the polynomial fits of the calculated lattice thermal conductivity.

difference is larger with more substitution. The increase of thermal conductivity above 1000 K is attributed to bipolar effect and the presence of impurity phase, consistent with the Seebeck and resistivity data. Finally, $Yb_{13.80}Sm_{0.19}Mn_{1.00}Sb_{11.02}$ has a maximum zT of 1.0 at 1275 K and the zT of $Yb_{13.50}Sm_{0.53}Mn_{1.06}Sb_{10.89}$ peaks at 0.9 at 1100 K.

Generally speaking, Sm and Pr substituted samples have similar thermoelectric properties. When more Pr or Sm is substituted into the structure, a higher electrical resistivity and a lower carrier concentration are expected. Decrease in lattice thermal conductivity can be observed when substitutions are in large amounts. Seebeck coefficients and effective band gap do not show clear tendency with increasing x and tend to initially improve and then remain stable. Overall effect is a limited range of zT values and $Yb_{13.82}Pr_{0.18}Mn_{1.01}Sb_{10.99}$ has the best zT values due to its slightly higher Seebeck coefficient. The substitution of RE^{3+} for Yb^{2+} increases the Seebeck coefficients, electrical resistivity and decreases the thermal conductivity. The initial decrease in carrier concentration upon RE^{3+} substitution is larger than expected suggesting that the single parabolic band model is too simplistic for this system. In addition, light *RE*s have partially filled *f*-levels that are nearer to the top of the Fermi level compared to Yb^{2+} *f*-levels, which may contribute to the band structure. Theoretical calculations on this complex structure will provide insight and help interpret this change.

Conclusions

$Yb_{14-x}RE_xMnSb_{11}$ (*RE* = Pr and Sm, $0 < x < 0.55$) were synthesized and characterized by PXRD and electron microprobe. Results of electron microprobe show the presence of the (Yb,*RE*)Sb impurity and that the amounts of Pr in the sample are lower than the preparative amounts. The presence of (Yb,*RE*)Sb and $(Yb,RE)_{11}Sb_{10}$ is apparent in the PXRD patterns after measurement, especially when the amounts of rare earth substitutions are high. Thermoelectric properties were measured on selected samples. In $Yb_{14-x}Pr_xMnSb_{11}$, carrier concentrations decrease with increasing Pr amounts in the samples thus the electrical resistivity increases. The Seebeck coefficients and effective band gaps initially increase and then remain stable. Thermal conductivity drops with substitution and the net effect is a large increase in zT values. $Yb_{13.82}Pr_{0.18}Mn_{1.01}Sb_{10.99}$ has the best maximum zT value of ~1.2 at 1275 K. Sm substituted samples show similar properties and $Yb_{13.80}Sm_{0.19}Mn_{1.00}Sb_{11.02}$ has its maximum zT of ~1.0 at 1275 K.

Acknowledgements

Part of this research was carried out at the Jet Propulsion Laboratory, California Institute of Technology, under a contract with the National Aeronautics and Space Administration. This work was supported by the NASA Science Mission Directorate's Radioisotope Power Systems. We also thank Jinfeng Zhao (UC Davis) for her help in SPS and Nick Botto (UC Davis) for his help in the electron microprobe. Financial support from NEUP is gratefully acknowledged.

References

1 U.S. Energy Flow Charts, Lawrence Livermore National Laboratory.
2 Fleurial, J.-P.; Bux, S.; Caillat, T. Engineering of Novel Thermoelectric Materials and Devices for Next Generation, Long Life, 20% Efficient Space Power Systems, In *Thermoelectric Devices and Systems*, Proceedings of the 11th International Energy Conversion Engineering Conference, San Jose, CA, July 14-17, 2013; American Institute of Aeronautics and Astronautics: Reston, VA, USA, 2013.
3 Riffat, S. B.; Ma, X. *Appl. Therm. Eng.* 2003, **23**, 913.
4 *CRC Handbbok of Thermoelectrics*; Rowe, D. M., Eds.; CRC press: Boca Raton, 1995.
5 Zhao, L. D.; Lo, S. H.; Zhang, Y.; Sun, H.; Tan, G.; Uher, C.; Wolverton, C.; Dravid, V. P.; Kanatzidis, M. G. *Nature (London, U.K.)* 2014, **508**, 373.
6 Hsu, K. F.; Loo, S.; Guo, F.; Chen, W.; Dyck, J. S.; Uher, C.; Hogan, T.; Polychroniadis, E. K.; Kanatzidis, M. G. *Science (Washington, DC, U.S.)* 2004, **303**, 818.
7 Korkosz, R. J.; Chasapis, T. C.; Lo, S. H.; Doak, J. W.; Kim, Y. J.; Wu, C. I.; Hatzikraniotis, E.; Hogan, T. P.; Seidman, D. N.; Wolverton, C.; Dravid, V. P.; Kanatzidis, M. G. *J. Am. Chem. Soc.* 2014, **136**, 3225.
8 Wu, H. J.; Zhao, L. D.; Zheng, F. S.; Wu, D.; Pei, Y. L.; Tong, X.; Kanatzidis, M. G.; He, J. Q. *Nat. Commun.* 2014, **5**, 4515.
9 Snyder, G. J.; Toberer, E. S. *Nat. Mater.* 2008, **7**, 105.
10 Rowe, D.; Min, G. *J. Mater.Sci. Lett.* 1995, **14**, 617.
11 Nolas, G. S.; Slack, G. A.; Schujman, S. B. Semiconductor Clathrates: A Phonon Glass Electron Crystal Material with Potential for Thermoelectric Applications. In *Semiconductors and Semimetals*; Terry, M. T., Ed.; Elsevier: Amsterdam, 2001; Vol. 69, pp 255-300.
12 Nolas, G. S.; Morelli, D. T.; Tritt, T. M. *Ann. Rev. Mater. Sci.* 1999, **29**, 89.
13 Kauzlarich, S. M.; Brown, S. R.; Snyder, G. J. *Dalton Trans.* 2007, 2099.
14 Chan, J. Y.; Olmstead, M. M.; Kauzlarich, S. M.; Webb, D. J. *Chem. Mater.* 1998, **10**, 3583.
15 Brown, S. R.; Kauzlarich, S. M.; Gascoin, F.; Snyder, G. J. *Chem. Mater.* 2006, **18**, 1873.
16 Möchel, A.; Sergueev, I.; Wille, H. C.; Juranyi, F.; Schober, H.; Schweika, W.; Brown, S. R.; Kauzlarich, S. M.; Hermann, R. P. *Phys. Rev. B* 2011, **84**, 184303.
17 Holm, A. P.; Kauzlarich, S. M.; Morton, S. A.; Waddill, G. D.; Pickett, W. E.; Tobin, J. G. *J. Am. Chem. Soc.* 2002, **124**, 9894.
18 Hu, Y.; Wang, J.; Kawamura, A.; Kovnir, K.; Kauzlarich, S. M. *Chem.Mater.* 2015, **27**, 343.
19 Sánchez-Portal, D.; Martin, R. M.; Kauzlarich, S. M.; Pickett, W. E. *Physical Review B* 2002, **65**, 144414.
20 Nesbitt, J. A. *J. Electron. Mater.* 2014, 43, 3128.
21 Paik, J-A; Brandon, E.; Caillat, T.; Ewell, R.; Fleurial, J.-P. Life Testing of $Yb_{14}MnSb_{11}$ for High Performance Thermoelectric Couples, In Proceedings of Nuclear and Emerging Technologies for Space 2011, Albuquerque, NM, Feb 7-10, 2011; Jet Propulsion Laboratory, National Aeronautics and Space Administration: Pasadena, CA, USA, 2011.
22 Rauscher, J. F.; Cox, C. A.; Yi, T.; Beavers, C. M.; Klavins, P.; Toberer, E. S.; Snyder, G. J.; Kauzlarich, S. M. *Dalton Trans.* 2010, **39**, 1055.
23 Yi, T.; Abdusalyamova, M. N.; Makhmudov, F.; Kauzlarich, S. M. *J. Mater. Chem.* 2012, **22**, 14378.
24 Brown, S. R.; Toberer, E. S.; Ikeda, T.; Cox, C. A.; Gascoin, F.; Kauzlarich, S. M.; Snyder, G. J. *Chem. Mater.* 2008, **20**, 3412.
25 Cox, C. A.; Toberer, E. S.; Levchenko, A. A.; Brown, S. R.; Snyder, G. J.; Navrotsky, A.; Kauzlarich, S. M. *Chem. Mater.* 2009, **21**, 1354.

26 Toberer, E. S.; Cox, C. A.; Brown, S. R.; Ikeda, T.; May, A. F.; Kauzlarich, S. M.; Snyder, G. J. *Adv. Func. Mater.* 2008, **18**, 2795.
27 Toberer, E. S.; Brown, S. R.; Ikeda, T.; Kauzlarich, S. M.; Jeffrey Snyder, G. *Appl. Phys. Lett.* 2008, **93**, 062110.
28 Uvarov, C. A.; Abdusalyamova, M. N.; Makhmudov, F.; Star, K.; Fleurial, J-P.; Kauzlarich, S. M. *Sci. Adv. Mater.* 2011, **3**, 652.
29 Yu, C.; Chen, Y.; Xie, H.; Snyder, G. J.; Fu, C.; Xu, J.; Zhao, X.; Zhu, T. *Appl. Phys. Exp.* 2012, **5**, 031801.
30 Uvarov, C. A.; Ortega-Alvarez, F.; Kauzlarich, S. M. *Inorg. Chem.* 2012, **51**, 7617.
31 Nolas, G.; Kaeser, M.; Littleton IV, R.; Tritt, T. *Appl. Phys. Lett.* 2000, **77**, 1855.
32 Morelli, D. T.; Meisner, G. P.; Chen, B.; Hu, S.; Uher, C. *Phys. Rev. B* 1997, **56**, 7376.
33 Lamberton, G. A.; Bhattacharya, S.; Littleton, R. T.; Kaeser, M. A.; Tedstrom, R. H.; Tritt, T. M.; Yang, J.; Nolas, G. S. *Appl. Phys. Lett.* 2002, **80**, 598.
34 Kuznetsov, V.; Kuznetsova, L.; Rowe, D. *J. Phys.: Condens. Matter* 2003, **15**, 5035.
35 Rodríquez-Carvajal, J. *Physica B.* 1993, **192**, 55.
36 Rodriguez-Carvajal, J.; Roisnel, T. WinPLOTR: A Windows Tool for Powder Diffraction Pattern Analysis, In *Materials Science Forum*, Proceedings of the Seventh European Powder Diffraction Conference, Barcelona, Spain, May 20-23, 2000; Delhez R., Mittemeijer E.J., Eds; Trans Tech Publications: Stafa, Switzerland, 2001, Vol. 378-381, pp 118-123.
37 Mccormack, J. A.; Fleurial, J.-P. Electrical Characterization of SiGe Thin Films. *Proceedings of the Modern Perspectives on Thermoelectrics and Related Materials Symposium*, Anaheim, CA, 1991, pp 135-141.
38 Borup, K. A.; de Boor, J.; Wang, H.; Drymiotis, F.; Gascoin, F.; Shi, X.; Chen, L.; Fedorov, M. I.; Müller, E.; Iversen, B. B. *Energy Environ. Sci.* 2015, **8**, 423.
39 Wang, H.; Porter, W. D.; Böttner, H.; König, J.; Chen, L.; Bai, S.; Tritt, T. M.; Mayolet, A.; Senawiratne, J.; Smith, C.; Harris, F.; Gilbert, P.; Sharp, J. W.; Lo, J.; Kleinke, H.; Kiss, L. *J.Electron.Mater.* 2013, **42**, 654.
40 Wood, C.; Zoltan, D.; Stapfer, G. *Rev. Sci. Instrum.* 1985, **56**, 719.
41 J. W. Vandersande, C. W., A. Zoltan and D. Whittenberger *Therm. Cond.* 1988, **19**, 455.
42 Ravi, V.; Firdosy, S.; Caillat, T.; Brandon, E.; Walde, K.; Maricic, L.; Sayir, A. *J. Electron. Mater.* 2009, **38**, 1433.
43 Grebenkemper, J. H.; Kauzlarich, S. M. *APL Mater.* 2015, **3**, 041503.
44 Dean, J. A.; Lange, N. A. *Lange's Handbook of Chemistry*; McGraw-Hill: New York, 1992.
45 Bodnar, R. E.; Steinfink, H. *Inorg. Chem.* 1967, **6**, 327.
46 Clark, H. L.; Simpson, H. D.; Steinfink, H. *Inorg. Chem.* 1970, **9**, 1962.
47 Samsonov G.V., Abdusalyamova M.N., and Shokirov K. Inorg. Mater. 1974, **10**, 790.
48 Brown, S. R.; Kauzlarich, S. M.; Gascoin, F.; Jeffrey Snyder, G. *J. Solid State Chem.* 2007, **180**, 1414.
49 Kawamura, A.; Hu, Y; Kauzlarich, S. M. submitted to *J. Electron. Mater.*
50 Grebenkemper, J. H.; Barrett, D.; Hu, Y.; Gogna, P.; Chen-Kuo Huang, C-K, Bux, S. K. and Kauzlarich, S. M. submitted to Chem. Mater.
51 Goldsmid, H. J.; Sharp, J. W. *J. Electron. Mater.* 1999, **28**, 869.
52 Xu, J.; Kleinke, H. *J. Comput. Chem.* 2008, **29**, 2134.
53 Fistul', V. I. *Heavily doped semiconductor*; Plenum: New York, 1969.
54 Caillat, T.; Fleurial, J.-P.; Borshchevsky, A. *J. Phy. Chem. Solids* 1997, **58**, 1119.